# Insight into Hydrazinium Nitrates, Azides, Dicyanamide, and 5-Azidotetrazolate Ionic Materials from Simulations and Experiments

Justin B. Hooper,*,[†] Oleg Borodin,[†,‡] and Stefan Schneider[§]

[†]Wasatch Molecular Inc., 2141 St. Marys Drive, Suite 102, Salt Lake City, Utah 84108, United States
[‡]Electrochemistry Branch, Army Research Laboratory, 2800 Powder Mill Road, Adelphi, Maryland 20783, United States
[§]Air Force Research Laboratory, 10 East Saturn Boulevard, Building 8451, Edwards Air Force Base, California 93524, United States

Ⓢ Supporting Information

ABSTRACT: A transferrable, polarizable, quantum chemistry (QC) based force field has been developed for hydrazinium ($N_2H_5^+$), monomethylhydrazinium ((CH_3)-$N_2H_4^+$), and dimethylhydrazinium ((CH_3)$_2N_2H_3^+$) cations in combination with the nitrate (NO_3^-), azide (N_3^-), dicyanamide ($N(CN)_2^-$), and 5-azidotetrazolate (CN_7^-) anions. Inclusion of the off-atom charge center to represent a lone pair on the hydrazinium-based cations significantly improved the electrostatic potential description around cations and led to overall a more accurate prediction of ionic crystal cell parameters in molecular dynamics (MD) simulations. Seven different ionic systems have been investigated: $[N_2H_5][NO_3]$, $[(CH_3)N_2H_4][NO_3]$, $[(CH_3)_2N_2H_3][NO_3]$, $[N_2H_5][CN_7]$, $[(CH_3)N_2H_4][N_3]$, $[(CH_3)_2N_2H_3][N_3]$, $[N_2H_5]$-$[N(CN)_2]$. For all but $[(CH_3)_2N_2H_3][NO_3]$ and $[N_2H_5][N(CN)_2]$, QC calculations of a single, gas-phase ion pair predicts spontaneous deprotonation of the cation. Crystal lattice parameters obtained from MD simulations for these seven ionic crystals were compared with the previously published experimental data as well as the crystal structure of $[N_2H_5][N(CN)_2]$ determined in this work from X-ray data. In general, MD simulations predicted crystal lattice vectors/angles (volumes) within a 5% (3%) absolute margin of error from experiments, with outlying volume deviations of 5–6.6% for three crystals $[(CH_3)N_2H_4][N_3]$, $[N_2H_5][NO_3]$, and $[(CH_3)N_2H_4][NO_3]$ with combinations of particularly small anions and/or cations. Structural comparisons between ionic materials in the liquid and crystalline states are made, including the observation of two crystalline systems where the crystalline state induces conformational changes in the methylated hydrazinium cations between the gas-phase and liquid states. Elastic constants and estimated shear and bulk moduli were extracted from MD simulations for all seven ionic crystals and correlated with the structural motifs of ion interactions in the crystals.
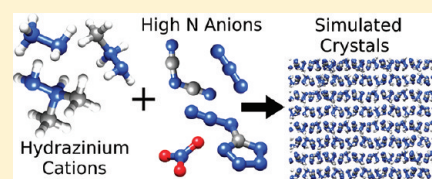
I. INTRODUCTION

Hydrazine, mixtures of hydrazine, or derivatives of hydrazine have been utilized for wide-ranging applications including polymer synthesis and processing, metal recovery and removal, pharmaceutical and agricultural applications, and bioactive applications such as herbicides and pesticides.[1] Perhaps the highest profile use for the hydrazine-based compounds, however, is provided by its long-standing role as a primary constituent of fuel systems for aerospace applications. Much research has been performed to elucidate the behavior of hydrazine and its methylated derivatives, monomethylhydrazine (MMH) and unsymmetric dimethylhydrazine (UDMH), by NASA[2,3] and others in order to understand and control the conversion of these high-energy chemicals into suitable energy sources for aerospace applications. Unfortunately, the properties that make hydrazine and derivatives desirable compounds for these applications (namely, high-energy density, low reaction threshold, and high volatility associated with the liquid state) also contribute to its potential for harm during uncontrolled release. Hydrazine, MMH, and UDMH have also been shown to be carcinogenic[4,5] in laboratory tests involving rodents and are suspected to have similar effects on humans via oral or vapor exposure.

Recently, ionic liquids (ILs) have attracted significant attention as solvent replacements[6,7] and alternatives to the hydrazine-based hypergolic propellant.[8–11] Due to their ionic nature, IL vapor pressure is low, resulting in reduced environmental impact. Moreover, existence of numerous cation–anion combinations provides an avenue for optimization of the thermodynamic properties and reaction pathways. Experimental synthesis and characterization of novel high nitrogen containing ionic liquids and crystals often show reactivity characteristics which make characterization and sometimes even handling difficult, adding to the challenges and safety risk for experimental investigation.[12–14] In cases such as these, the ability to accurately predict/describe the thermodynamic response of these compounds without the associated risks of experimental measurements is of obvious utility. Structural and thermodynamic behavior of the material can be quantitatively predicted given an accurate force field description and proper simulation methodology. We have recently demonstrated the ability of our force field development
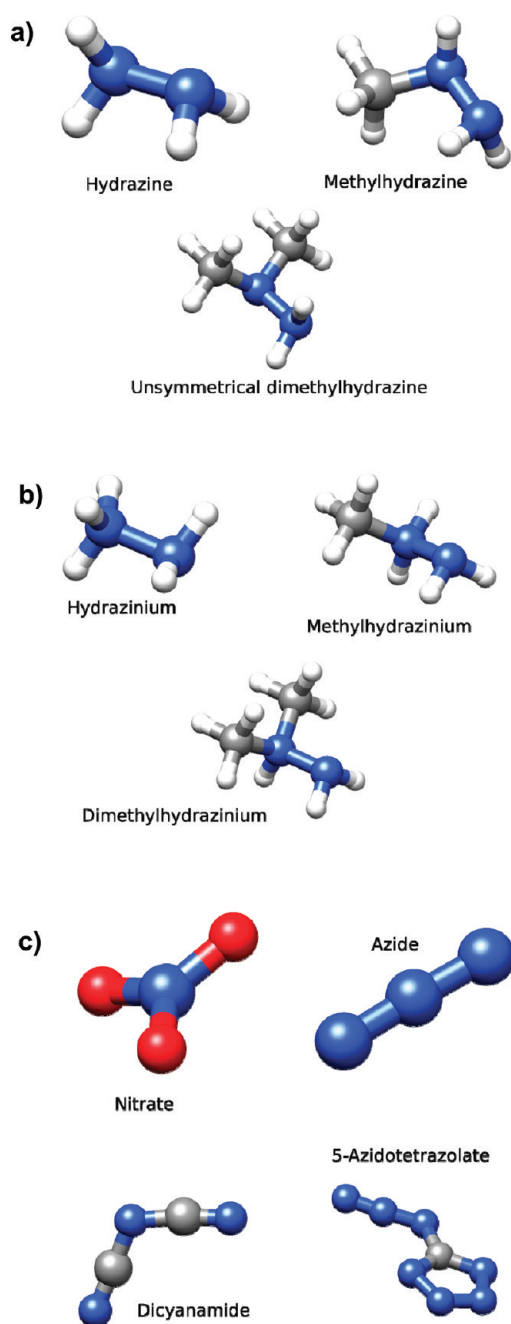
Figure 1. Schematics for the neutral hydrazines (a) used as a basis for the hydrazinium cations (b) as well as for the anions (c) employed in this work.

and simulation process to provide models that can accurately predict density, heat of vaporization, ion diffusion coefficient, ionic conductivity, and viscosity of a diverse class of ionic liquids.[15] The same process also has produced force fields which have accurately predicted ionic crystal lattice parameters for four ionic crystals[15] as well as prediction of lattice parameters, electrical conductivity, and melting point of a plastic crystalline system.[16] Recently Maginn's group has shown[17] that it is quite difficult to achieve an accurate and consistent description of the modified hydrazinium nitrate ionic crystals. In this work, we undertake the challenge of developing a systematic force field that will describe crystal structures for these modified hydrazinium nitrate

ionic materials. Furthermore, the developed polarizable force field will be extended to other high nitrogen content anions: azide (N_3^-), dicyanamide $(N(CN)_2^-)$, and 5-azidotetrazolate (CN_7^-) in addition to NO_3^-. Due to a lack of liquid-state thermodynamic data, validation will be performed using seven high nitrogen content ionic crystals. Finally, molecular dynamics (MD) simulations are performed using the developed force field to provide initial investigations of the mechanical properties in the crystalline system as well as the structural interactions of cations and anions in the crystalline (and in some cases liquid) state.

The primary difficulty in developing a force field for the high nitrogen content IL salts is a lack of thermodynamic information in the liquid phase, which is often unstable for hydrazinium-based ionic liquids. Therefore, we rely heavily on the crystal structures of the hydrazinium-based ionic crystals for force field validation. Starting from a description of the neutral hydrazines, we refine our force field to produce the best *overall* description over the entirety of the crystal structures investigated, using a single consistent force field, with the idea being that a consistent set of potential interactions for a number of ionic crystals with different crystal symmetries, melting temperatures, and ionic species will provide sufficient statistical variance over the hydrazinium-based ions to allow us to gauge the predictive ability of a hydrazinium force field for use in the generic case.

To this end, we have investigated three substituted forms of hydrazine, in both their neutral and singly charged cationic states: Hydrazine and its cation (hydrazinium, $N_2H_5^+$), monomethylhydrazine (MMH) and its cation (methylhydrazinium, $(CH_3)N_2H_4^+$), and the unsymmetric dimethylhydrazine (UDMH) and its cation (1,1-*N,N*-dimethylhydrazinium, $(CH_3)_2N_2H_3^+$). Representations of the individual neutral molecules are presented as Figure 1a, while the cationic forms are presented as Figure 1b. In the case of the cationic forms, we have investigated a number of ionic crystals which utilize four common, singly charged nitrogen containing anions: Nitrate (NO_3^-), azide (N_3^-), dicyanamide $(N(CN)_2^-)$, and 5-azidotetrazolate (CN_7^-), shown in Figure 1c. Note that CN_7^- has one of the highest known nitrogen contents and was only recently characterized in detail.[12] For NO_3^-, crystal structures with all three hydrazinium cations are available in the literature.[18,19] For N_3^-, only crystal structures involving the methylated cations $((CH_3)N_2H_4^+$ and $(CH_3)_2-N_2H_3^+)$ were available.[20,21] Both $N(CN)_2^-$ and CN_7^- were investigated with only $N_2H_5^+$, with the latter crystal structure taken from ref 12. The crystal structure of the $[N_2H_5][N(CN)_2]$ system was derived via X-ray diffraction analysis, with the procedure outlined in the Supporting Information for this paper, while the crystal structure itself is available through the Cambridge Crystallographic Data Center (CCDC) as structure 821616.

The remainder of the paper is organized as follows: In section II the force field development is outlined, while in section III we discuss simulation methodology. Section IV presents the results, while interpretation and conclusions are provided in section V.

II. FORCE FIELD DEVELOPMENT

Force Field Functional Form. The following form of the force field relating the potential energy $U^{tot.}(\mathbf{r})$ to atomic coordinates $\mathbf{r}$ for the ensemble of atoms has been chosen. It is split into nonbonded

13579

dx.doi.org/10.1021/jp2044064 |*J. Phys. Chem. B* 2011, 115, 13578–13592

$U^{NB}(\mathbf{r})$ and bonded contributions as follows:

$$U^{tot.}(\mathbf{r}) = U^{NB}(\mathbf{r}) + \sum_{bends} U^{bend}(\theta_{ijk}) + \sum_{dihedrals} U^{dihedral}(\phi_{ijkl})$$
$$+ \sum_{\substack{improper \\ dihedrals}} U^{imp.}(\theta_{ijkl}^{imp.}) \tag{1}$$

where the sums are over all bends, dihedrals, and improper dihedrals in the system. The contributions of each of these terms, respectively, are calculated as follows:

$$U^{bend}(\theta_{ijk}) = \frac{1}{2} k_{\alpha\beta\gamma}^{bend}(\theta_{ijk} - \theta_{ijk}^0)^2 \tag{2}$$

$$U^{dihedral}(\phi_{ijkl}) = \sum_n \frac{1}{2} k_{\alpha\beta\gamma\delta,n}^{dihedral}[1 - \cos(n\phi_{ijkl})] \tag{3}$$

$$U^{imp.}(\phi_{ijkl}^{imp.}) = \frac{1}{2} k_{\alpha\beta\gamma\delta}^{imp.}(\phi_{ijkl}^{imp.})^2 \tag{4}$$

where θ_{ijk} and θ_{ijk}^0 are the instantaneous and natural bending angles for atoms i, j, and k; ϕ_{ijkl} is the dihedral angle for atoms i, j, k, and l; and $\phi_{ijkl}^{imp.}$ is the out-of-plane bending angle for an sp^2 center at atom j. The strength of these interactions is characterized by the corresponding force constants: $k_{\alpha\beta\gamma}^{bend}$, $k_{\alpha\beta\gamma\delta}^{dihedral}$, and $k_{\alpha\beta\gamma\delta}^{imp.}$, respectively, where the subscripts α, β, γ, and δ represent the atom type for atoms i, j, k, and l, respectively. There are no bond energy terms due to the fact that bonds are always constrained at a bond specific fixed distance.

$U^{NB}(\mathbf{r})$ is generated by summing the two-body repulsion and dispersion energy terms $[U^{RD}(\mathbf{r})]$, the energy due to interactions of fixed charges $[U^{coul}(\mathbf{r})]$, and the polarization energy $[U^{pol.}(\mathbf{r})]$, arising from the interaction between induced dipoles with both fixed charges and other induced dipoles:

$$U^{NB}(\mathbf{r}) = U^{RD}(\mathbf{r}) + U^{coul}(\mathbf{r}) + U^{pol.}(\mathbf{r})$$
$$= \sum_{i>j} \left(A_{\alpha\beta} \exp(-B_{\alpha\beta}r_{ij}) - \frac{C_{\alpha\beta}}{r_{ij}^6} + D\left(\frac{12}{B_{\alpha\beta}r_{ij}}\right)^{12} \right)$$
$$+ \sum_{i>j} \left(\frac{q_i q_j}{4\pi\varepsilon_0 r_{ij}} \right) - \frac{1}{2}\sum_i \vec{\mu}_i \cdot \vec{E}_i^0 \tag{5}$$

where $\vec{\mu}_i = \alpha_i \vec{E}_i^{tot.}$ is an induced dipole at force center i, α_i is the isotropic atomic polarizability, $\vec{E}_i^{tot.}$ is the total electrostatic field at the atomic site i due to permanent charges q_j and induced dipoles $\vec{\mu}_j$, ε_0 is the dielectric permittivity of vacuum, $\vec{E}_i^0$ is the electric field due to fixed charges only, and $A_{\alpha\beta}$ and $B_{\alpha\beta}$ are the repulsion parameters and $C_{\alpha\beta}$ the dispersion parameter for interaction between atoms i and j with atom types α and β. The term $D(12/B_{\alpha\beta}r_{ij})^{12}$, with $D = 5 \times 10^{-5}$ kcal/mol for all pair interactions not involving a lone pair force center, is essentially zero at typical nonbonded atomic separations but becomes the dominant term at $r_{ij} < 1$ Å, ensuring that $U^{RD}(\mathbf{r})$ is repulsive at distances much smaller than the size of an atom. Intramolecular nonbonded interactions are included for atoms separated by three or more covalent bonds. We have utilized Thole screening[22] ($a_T = 0.2$), which locally damps induced-dipole—induced-dipole interactions over a short spatial range, helping to prevent the occurrence of the "polarization catastrophe" wherein unphysical behavior can occur at relatively small interatomic distances due to the pointlike nature of the dipole—dipole interaction.[23] Additionally, an 80% reduction is applied to

intramolecular interactions between an induced dipole and a partial charge separated by exactly three bonds. Finally, for heteroatom interactions, the modified Waldman—Hagler combining rules were used:

$$A_{ij} = \sqrt{A_{ii}A_{jj}} \frac{B_{ij}^6}{B_{ii}^3 B_{jj}^3}$$
$$B_{ij} = \left(\frac{2}{B_{ii}^{-6} + B_{jj}^{-6}} \right)^{1/6} \tag{6}$$
$$C_{ij} = \sqrt{C_{ii}C_{jj}}$$

These combining rules have been successfully used by us for simulations of liquids, polymers, electrolytes, and ionic liquids.[15] A, B, and C parameters link the functional form of the repulsion/dispersion term of eq 5 to the physically meaningful quantities of potential well depth (ε), the interatomic separation at the potential minimum (R^*), and the steepness parameter (λ) as given by

$$A = 6\varepsilon(exp\,\lambda)/(\lambda - 6) \tag{7}$$

$$B = \lambda/R^* \tag{8}$$

$$C = \varepsilon\lambda(R^*)^6/(\lambda - 6) \tag{9}$$

Partial Atomic Charges. Partial atomic charges are based on the electrostatic potentials of the gas-phase molecules calculated on a grid of evenly spaced points ($\sim 10^5$ points) around each molecule in the lowest energy gas-phase conformations, with a small weighting (10%) also given to the dipole moment ($\vec{\mu}_i$) of the molecule. The electrostatic potential for cationic and neutral molecular was calculated at the MP2/aug-cc-pvDz level, while the electrostatic potential for the anions was calculated at the MP2/cc-pvTz level. Charge—bond increments are used to calculate partial atomic charges, where the value (q_i) of the partial charge positioned on atom i is calculated as the sum of all charge—bond increments that involve atom i:

$$q_i = \sum_{j=1}^{N_{bond}} \delta_{ij} \tag{10}$$

with δ_{ij} being the charge—bond increment connecting an atom of type i to an atom of type j. The set of charge—bond increments for the overall molecule is determined by minimizing the objective function:

$$\chi^2(\vec{\delta}) = \sum_{i=1}^{M} \left[\sum_{j=1}^{N_{grid}} \frac{\omega^\phi}{N_{grid}}(\phi_{ij}^{QC} - \phi_{ij}^{FF}(\vec{\delta}))^2 + \omega^{\vec{\mu}}(\vec{\mu}_i^{QC} - \vec{\mu}_i^{FF}(\vec{\delta}))^2 \right] \tag{11}$$

where ϕ_{ij}^{QC} and ϕ_{ij}^{FF} are the electrostatic potential for the ith molecule (or complex) at the jth grid point from quantum chemistry (QC) and the developed force field (FF), respectively, $\vec{\mu}_i^{QC}$ and $\vec{\mu}_i^{FF}$ are the dipole moments, and ω^ϕ and ω^μ are the relative weights for fitting the electrostatic potential and the dipole moments, respectively. The electrostatic potential weighting was set to 1.0, with the dipole weighting set to 0.1 for all systems. All points within 1.8 Å of an oxygen atom, 1.5 Å of a hydrogen atom, 2.5 Å of a carbon atom, or 2 Å of a nitrogen atom or further from any atom than 4 Å were excluded from the fitting. For the dicyanamide, nitrate, and azide anions, this process is sufficient to yield a FF approximation that
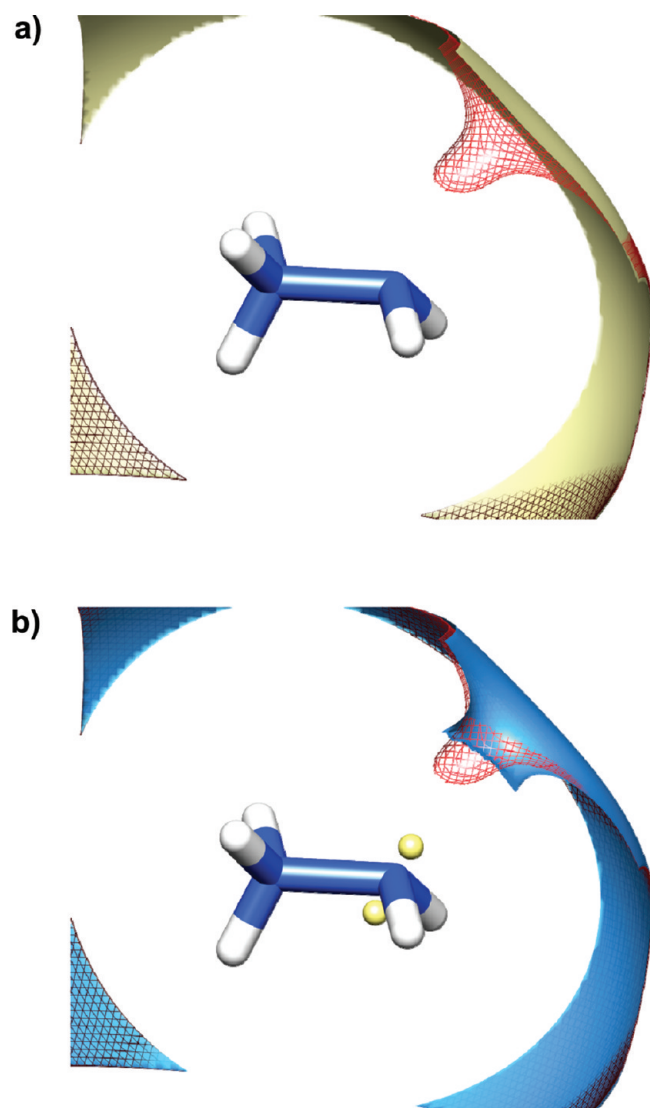
Figure 2. Representation of the difference in the shapes of the force field derived (solid) and quantum chemistry calculated (MP2/aug-cc-pvDz, mesh) electrostatic surfaces at 0.125 eV for the hydrazinium cation without (a) and with (b) explicit lone pairs. The complete inability of the system without lone-pairs to even qualitatively capture the electrostatic potential well near the tetrahedral position of the NH_2 group is evident, with the force field derived potential surface in part b clearly descending toward the lone pairs (represented by yellow spheres).

Figure 3. Comparison of potential isosurfaces at a value of -0.15 eV for the $[CN_7]$ anion. Quantum chemistry calculations are represented by the green mesh, while those for the forcefield without (red solid) and with (light blue, solid) lone pairs are superimposed. There are five planar lone pair force centers: One each on the ring nitrogens, with the 5th attached to the C—N—N bend attaching the tetrazole ring to the azide tail.

accurately reproduces the electrostatic potential of the molecules calculated via QC. However, for all of the hydrazinium cations as well as 5-azidotetrazolate, fitting charges situated only at atom centers yielded unsatisfactory results in the reproduction of the electrostatic potential around a molecule. In these cases, the addition of charges positioned at off-atom force centers to act as additional degrees of freedom for the charge fitting routine significantly improved the electrostatic potential fit. These charge centers were assigned zero mass and no repulsion—dispersion interactions. The electrostatic force acting on the dummy force center is distributed to its attached triatomic basis using the chain rule.[24]

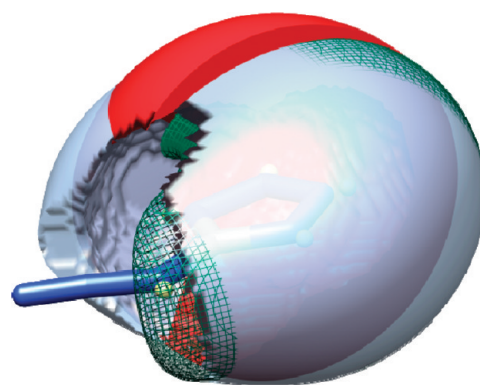The importance of including the lone pairs for accurate reproduction of the local electrostatic potential of the hydrazinium cations is depicted via Figure 2. When the additional off-atom charges emulating lone pairs are removed, the potential near the NH_2 end of the molecule is smooth, as shown in Figure 2a. The QC, on the other hand, shows a marked depression in local electrostatic potential (which shows up as a "well" in a constant potential isosurface as plotted in Figure 2) in a position which is commensurate with the location of an expected tetrahedral lone pair attached to the nitrogen in the NH_2 group. In Figure 2b, we present a comparison of the electrostatic potential surfaces for the hydrazinium cation with the addition of two off-atom positioned charges. Addition of the lone pair representing charges yields a far better approximation of the quantum chemistry based electrostatic potential, reproducing a substantial portion of the potential well in the vicinity of the nitrogen atoms. It should be noted that the protruding "finger" of the QC-derived potential isosurface that extends further toward the nitrogen in Figure 2b is due to the fact that the range of the QC surface actually impinges on the excluded radius (2 Å) of the nitrogen atom in the partial charge calculation (placing it well into the repulsive core of the nitrogen atom). In quantitative terms, the introduction of the additional off-atom-centered charges to the NH_2 group lowers the mean square deviation of the electrostatic energy from initial values of 1.49, 1.23, and 0.98 kcal/mol to 0.77, 0.77, and 0.78 kcal/mol for $N_2H_5^+$, $(CH_3)N_2H_4^+$, and $(CH_3)_2N_2H_3^+$, respectively. Interestingly, if we simply add a single off-atom charge oriented outward in the direction of the observed QC well and calculate the charge fit, the results are only marginally better than for no lone pairs. Thus, addition of the off-atom-center charge in the location of the expected lone-pair electron clouds is not nearly as effective for improving the description of electrostatic potential around these molecules as addition of the inward and outward positioned charge centers. One can draw a parallel with the TIP4P water model[25] that has an additional force center inward of the H—O—H bend, in the direction opposite of the lone pair.

In the 5-azidotetrazolate anion as well, lone pairs significantly improve the reproduction of the electrostatic potential near the molecule. Here, however, the influence of the additional off-atom-centered charges on the electrostatic potential is subtler in nature. As shown by Figure 3, initial predictions of the electrostatic

potential around the tetrazolate ring without the additional charges yields a potential that, at any constant value, is more spherical in character (red surface) than that predicted by quantum chemistry (green mesh). Due to the aromatic nature of the nitrogen in the ring (as well as the resonant nature of the azide nitrogen connected to the ring's single carbon atom), we expect that lone-pair electrons in this molecule will be in the plane of the ring and have therefore added planar lone-pair centers to each ring nitrogen as well as the azide nitrogen connected to the ring carbon. The resultant potential fit to the quantum chemistry is shown by the blue surface in Figure 3. With the additional lone pairs, the force field becomes more planar, better reproducing the quantum chemistry data with only a small bit of the "cusp" near the azide—carbon bond not well accounted for. Here, the initial mean square deviation between electrostatic potential from FF and QC calculations was 3.14 kcal/mol, while inclusion of explicit lone pairs lowers this to 1.00 kcal/mol.

Atomic Polarizabilities. Isotropic atomic polarizabilities are calculated from both the gas-phase molecular polarizabilities and the binding energies of a molecule with a test charge performed at the MP2/aug-cc-pvDZ (MP2/cc-pvTz) level of theory. While it is generally accepted that the addition of diffuse functions is important for accurate prediction of polarization response in the gas phase, and to a smaller extent charge distribution, it has been observed that use of full gas-phase polarizabilities in condensed-phase simulation may not provide the best thermodynamic prediction in condensed phases. For example, using gas-phase polarizabilities in the construction of a Drude-based water model has been shown to lead to overprediction of the dielectric constant,[26] while the polarizability of the Cl^- anion in aqueous solution was estimated to be just 63% of the gas-phase value.[27] We have therefore intentionally used nonaugmented basis sets to counter the overprediction of condensed-phase polarizability, an approach that has previously been successful both for our[28] and other groups[29] simulations with polarizable force fields.

The atomic polarizability was assumed to be transferable for atoms located in the same chemical environment that is bound to the same chemical elements. This approach has yielded good results for a number of previous investigations.[15,31] Polarization interactions between atoms separated by one or two bonds are assumed to be subsumed within the bond and bend, respectively, and are therefore excluded from our calculations. The developed force field predicted molecular polarizability of the cations within 5% of the QC values, with $N_2H_5^+$ having a value of 2.48 Å³ (QC = 2.53 Å³), $(CH_3)N_2H_4^+$ at 4.13 Å³ (QC = 4.35 Å³), and $(CH_3)_2N_2H_3^+$ 5.80 Å³ from force field calculations vs a QC value of 6.00 Å³.

For the anionic species, we fit only the azide and CN_7^- anions, since $N(CN)_2^-$ and NO_3^- were previously fit.[15] We first fit the polarizability of the azide anion using a teardrop-shaped charge path both along and at a 45° angle to the principal axis of the molecule, yielding a calculated molecular polarizability of 3.37 Å³ for the force field vs 3.39 Å³ for the QC. We then utilized these polarizabilities directly for the azide tail of the CN_7^- molecule, as well as transferring the terminal nitrogen polarizability from the azide to the CN_7^- ring nitrogens since both molecules are comprised of resonant anionic nitrogen atoms. The resultant molecular polarizabilities for CN_7^- predicted by the force field was 8.65 Å³ compared to the QC value of 11.35 Å³. Attempts to increase the molecular polarizability to more accurately represent the quantum values provided a dilemma: We could easily increase the value of the polarizability, but only at the expense

of the quality of fit to the overall electrostatic potential. The as-transferred parameters were found to yield the best fit of the electrostatic potential, yielding underprediction of the molecular polarizability by ~25%. This level of reduction in the overall molecular polarizability has been found to be necessary in previous simulations that were able to accurately reproduce the crystal structure of the TATB molecular crystal.[32] It is noteworthy that TATB also represents a molecular system comprised of resonant ring structures with the presence of strong hydrogen bonding.

Valence and Dihedral Parameters. Due to the fact that bond fluctuations would lead to rapid fluctuation of the local electrostatic field, necessitating significantly more calculation effort under the polarizability model implemented in this framework, bond lengths were constrained at a fixed value in the MD simulations. Values for the fixed bonds were provided by single-molecule QC calculations at the MP2/aug-cc-pvDz (neutral and cations) and MP2/cc-pvTz (anions) theory level. Triple-ζ basis sets for anions were chosen over double-ζ due to their ability to consistently better represent the bond lengths observed via X-ray measurement of the ionic crystals.

The natural bending angles (θ_{ijk}^0) were fit to the optimized QC geometries, with angles in common chemical environments constrained to have the same force field parameters across instances where the angle's central atom is bonded to the same elements, in the same nominal charge state, in the same or symmetrically equivalent orders. For example, one set of common angular parameters is utilized for the H—N—H angle of the NH_2 group bonded to the substituted nitrogen in neutral hydrazines, regardless of methylation state, while another set of common angular parameters is used for the same bend bonded to the formally +1 nitrogen of the hydrazinium cations, again regardless of methylation state.

The torsional (dihedral) parameters are fit to energies from MP2/aug-cc-pvDz (MP2/cc-pvTz) level scans of the dihedral angle(s) of the cations (anions), in 10° increments, up to the maximum symmetry-reduced angle, with the remainder of the molecular degrees of freedom allowed to relax. To reproduce the inversion energy (barrier) for the N—N*H_2 group and dihedral scans, simultaneous adjustment of the dihedral parameters and the bending parameters was performed.

Repulsion—Dispersion Parameters. Fitting repulsion—dispersion (R/D) interaction parameters (A—C in eq 6 or, equivalently, ε, λ, and R^* in eqs 7—9) is the most challenging and controversial part of force field development, since the parameters can be obtained by fitting to a number of different data sets yielding somewhat different potentials. The most often used data for fitting the repulsion dispersion parameters are crystal structures together with sublimation energies, liquid densities, and heats of vaporization (ΔH^{vap}), vapor—liquid equilibrium data, and gas-phase dimer binding energies obtained from QC calculations. In previous work we have fit the R/D parameters to the density and ΔH^{vap} of nonionic liquids, while the density and dynamic properties were used for IL specific parameters.[15] Despite this approach working very well for previously characterized systems, it is intractable for our current investigation due to the dearth of information concerning dynamic properties of most of the ILs investigated. In general, due to the energetic nature of these compounds, little experimental data are known regarding dynamic properties for the ionic compounds in the liquid state. Thus, we have fit R/D potentials of the ionic forms via transferring them from the nonionic precursors, which have in turn been fit primarily on the basis of reproducing the liquid-state densities and ΔH^{vap} for

clear precursors where available (e.g., the substituted hydrazines) or for an unambiguously functionalized derivative (e.g., 1-azido-butane for the azide). The sole exception to this was the fitting of the (heavily screened) N^+ homoatomic potential, which has been generated by rescaling the neutral nitrogen R/D potential as discussed previously.[15] For DCA^- and NO_3^-, full parametrizations of good accuracy were available from previous efforts with differing cationic species.[15,16]

Cation–Anion Complexes. We have not investigated the ability of the developed force field to reproduce alkyl hydrazinium nitrate cation–anion binding energies because we found in the gas-phase the neutral analogues were most stable. Specifically, the geometry optimization performed at the MP2/cc-pvTz level starting with the cation–anion configurations of $[N_2H_5][NO_3]$, $[N_2H_5]$-$[CN_7]$, $[(CH_3)N_2H_4][NO_3]$, $[(CH_3)N_2H_4][N_3]$, and $[(CH_3)_2$-$N_2H_4][N_3]$ yielded the neutral molecular complexes. For the $[(CH_3)_2N_2H_3][NO_3]$ complex the nitrate anion and dimethylhydrazinium cation jointly share the proton in the minimum energy configuration, while only in the hydrazinium/dicyanamide system do the cation and anion retain their ionized nature in the gas phase.

For $[N_2H_5][NO_3]$, we performed additional QC calculations with a polarizable continuum model (using the integral equation formalism variant),[33] calculating $[N_2H_5][NO_3]$ pair interactions within a solvent cavity that is, in turn, embedded in a continuum model background with the dielectric properties of acetone. In this regime, a hydrazine/nitric acid pair at the interaction distances and geometries generated from minimization in the gas phase undergoes ionization, regenerating the expected $[N_2H_5][NO_3]$ ion pairing. Geometry optimization of $([N_2H_5][NO_3])_2$ starting from the neutral complex resulted in a spontaneous ionization in accord with results recently reported by Izgorodina et al. for acetic acid, to a range of amines.[34] However, in the later work, usage of PCM was not sufficient to ionize acetic acid –amine in the gas phase but ionization occurred in calculations with an explicit solvent.

Force field parameters are available to academic groups for noncommercial research and government laboratories at no cost upon signing a license agreement from Wasatch Molecular Inc.[35]

III. SIMULATION METHODOLOGY

Simulations in both the crystalline and liquid phases have been carried out with the Lucretius[36] molecular simulation package. Periodic boundary conditions were used in all simulations, with covalent bond lengths constrained using the velocity–Verlet form of the SHAKE algorithm.[37] The Ewald summation method was used for the treatment of long-range electrostatic forces between partial charges, as well as between partial charges and induced atomic dipoles, while direct induced-dipole–induced-dipole interactions were calculated only via an iterative real-space summation. The number of reciprocal Ewald vectors was chosen to satisfy the condition $k_i \geq L_i/2\pi$ with k_i being the number of Ewald vectors and L_i the total length of the simulation cell along lattice vector i, with $\alpha = 0.23$ used for the real-space decay factor. The number of ion pairs varied from 160 to 384, yielding periodic cell lengths of 30–40 Å, with the particular value between these limits dictated by the size of the crystalline unit cell. The MD simulations employed a multi-time-step reversible reference system propagator algorithm,[38] with a time step of 0.5 fs for bend vibrations and a time step of 1.0 fs for dihedral, out-of-plane deformation, repulsion–dispersion (van der Waals) interactions, and the real part of Ewald within a 7 Å cutoff. A time step of 2.0 fs was used for all interactions within an 11 Å cutoff including the

Table 1. Comparison between Experimental and Simulated Densities and Enthalpies of Vaporization for the Neutral Hydrazine and Azide Liquids

	for T = 298 K			
	N_2H_4	$(CH_3)N_2H_3$	$(CH_3)_2N_2H_2$	1-azidobutane
density (kg/m³)				
experiment	1003.6	870	791	883
simulation	1008.7	871	800	881
Δ (%)	0.5	0.1	1.1	0.2
ΔH^{vap} (kcal/mol)				
experiment	10.68	9.68	8.42	9.17
simulation	10.68	9.77	8.09	9.27
Δ (%)	0.0	0.9	−3.9	1.1

reciprocal part of Ewald and many-body polarization. A fourth-order polynomial tapering function was employed to drive the induced-dipole–induced-dipole interactions to zero at this cut-off, with tapering starting at 10.2 Å.

A combined MD–Monte Carlo (MD-MC) approach[39,40] was utilized to obtain crystal relaxation at 1 atm pressure and the appropriate temperatures for comparison to experimentally available crystal structures. In all cases, the experimentally derived crystal coordinates were used as a starting configuration for the MD-MC runs. The MD-MC technique consists of two iterating steps: First, a 500 fs trajectory segment of canonical ensemble MD simulation (NVT-MD) is performed, followed by a series of 10 attempted changes to the simulation cell shape and volume via isobaric–isothermal rigid molecule Monte Carlo (NPT-MC) moves that consisted of changing cell parameters. The combined NVT-MD and NPT-MC steps comprise a single iteration, with the input for each iteration coming from the results of the previous iteration. A total of 5000 iterations were performed for each MD-MC run, generating 50 000 attempted MC volume changes and 2.5 ns of composite trajectory time. All crystals were simulated for at least two such production runs, yielding a total simulation time of at least 5 ns. In all cases, the evolution of the lattice vectors and angles were monitored over time to ensure that they have stabilized at representative values for the system being simulated, with simulation calculations taken only from the latter 2 ns or more of the simulation after the lattice quantities are stabilized.

IV. SIMULATIONS RESULTS AND DISCUSSION

Liquid Density and Heat of Vaporization of Neutral Precursors. Comparisons between measured values and MD simulation results for liquid density and heat of vaporization of the neutral hydrazines,[1,41,42] as well as the precursor 1-azidobutane[43] used to parametrize our azide anion, are presented in Table 1. All of the molecules have been investigated at 298 K and 1 atm of pressure, with the resulting predictions for both density and ΔH^{vap} being quite accurate. Particular attention has been paid to accurate reproduction of the decreasing trend of ΔH^{vap} with the addition of subsequent methyl groups in the hydrazine system. For the azide group, in addition to fitting well both the density and ΔH^{vap} of 1-azidobutane, the azide group in anionic form has also recently been found to accurately reproduce densities and dynamic properties in concert with imidazolium-based cations.[44]

13583

dx.doi.org/10.1021/jp2044064 |*J. Phys. Chem. B* 2011, 115, 13578–13592

Table 2. Comparison between Predicted and Observed Densities (kg/m^3) of the Hydrazine Liquid Force Field at Elevated Temperatures

	N$_2$H$_4$		(CH$_3$)N$_2$H$_3$			(CH$_3$)$_2$N$_2$H$_2$		
	T = 299.75 K	T = 366.47 K	T = 308.15 K	T = 333.15 K	T = 343.15 K	T = 273.2 K	T = 310.26 K	T = 338.73 K
experiment	1003	940	858	834	824	812	773	742
simulation	1007	916	846	815	801	827	786	753
Δ (%)	0.4	−2.5	−1.5	−2.3	−2.8	1.8	1.7	1.5

Table 3. Comparison between Experimentally Observed and Simulated Crystal Structures (Lattice Vectors, Å; Lattice Angles, deg; Cell Volume, Å^3)

	⟨a⟩	⟨b⟩	⟨c⟩	⟨α⟩	⟨β⟩	⟨γ⟩	⟨vol⟩
[N$_2$H$_5$][NO$_3$]							
experiment	7.965	5.657	8.122	90.00	91.34	90.00	365.854
simulation	7.44	5.97	7.75	91.33	92.55	89.88	343.370
Δ (%)	−6.6	5.4	−4.6	1.5	1.3	−0.1	−6.1
[(CH$_3$)N$_2$H$_4$][NO$_3$]							
experiment	3.779	11.342	11.107	90.000	99.086	90.000	470.147
simulation	3.96	10.71	11.30	90.08	100.61	90.04	471.34
Δ (%)	4.9	−5.6	1.7	0.1	1.5	0.0	0.3
[(CH$_3$)$_2$N$_2$H$_3$][NO$_3$]							
experiment	14.039	5.649	7.603	90.000	90.000	90.000	602.958
simulation	14.48	5.56	7.37	89.69	89.76	89.99	593.61
Δ (%)	3.1	−1.5	−3.1	−0.3	−0.3	−0.0	−-1.6
[N$_2$H$_5$][CN$_7$]							
experiment	10.811	7.464	7.668	90.000	101.437	90.000	606.469
simulation	10.79	7.47	7.49	89.78	101.15	90.08	592.03
Δ (%)	−0.2	0.0	−2.3	−0.3	−0.3	0.1	−2.4
[(CH$_3$)N$_2$H$_4$][N$_3$]							
experiment	9.963	5.132	9.228	90.000	90.000	90.000	471.773
simulation	10.42	4.84	8.67	89.88	90.02	90.03	437.25
Δ (%)	4.6	−5.6	−6.1	−0.1	0.0	0.0	−7.3
[(CH$_3$)$_2$N$_2$H$_3$][N$_3$]							
experiment	8.445	7.042	10.075	90.000	108.321	90.000	568.741
simulation	8.49	7.18	10.04	88.50	108.90	90.69	578.29
Δ (%)	0.5	1.9	−0.3	−1.7	0.5	0.8	1.7
[N$_2$H$_5$][N(CN)$_2$]							
experiment (Pnma)	6.581	9.000	7.497	90.000	90.000	90.000	444.033
experiment (Cmcm)	6.568	8.983	7.484	90.000	90.000	90.000	441.559
simulation	6.82	8.89	7.31	90.06	90.03	89.88	443.62
Δ$_{Pnma}$ (%)	3.7	−1.2	−2.5	0.1	0.0	−0.1	−0.1
Δ$_{Cmcm}$ (%)	3.8	−1.0	−2.3	0.1	0.0	−0.1	0.5

We have also calculated the density response for the neutral hydrazine molecules as a function of temperature (at 1 atm pressure), which are shown in Table 2. For hydrazine, density parity at room temperature is quite good, but as the system heats the simulated systems expand more quickly than experimental observations. For the singly methylated molecule, we obtain reasonable density agreement (∼2.5%) for the ranges tested, which all reside below the boiling point of the liquid (361 K). Even better agreement between simulation and experiment is seen for UDMH, with simulations up to slightly above the boiling point of 336 K falling within a density variation of ∼1.5%.

Crystal Lattice Parameters. The lattice parameters of simulated crystals were compared with experiment for seven crystals: [Hyd][NO$_3$],[18] [MeHyd][NO$_3$],[19] [DiMeHyd][NO$_3$],[19] [MeHyd]-[N$_3$],[20] [DiMeHyd][N$_3$],[21] [Hyd][N(CN)$_2$], and [Hyd][CN$_7$].[12] For the entire test set simulated, we find generally good agreement between the simulated crystals and those obtained from experimental investigations, as summarized in Table 3. With the exceptions of [Hyd][NO$_3$] and [MeHyd][N$_3$], cell volumes vary by less than 3%, with the former deviating by −6 and −7.1%, respectively. Individual lattice vectors obtained from MD simulations show deviations from experiments generally falling in the range of 6% absolute deviation or less, while lattice angles
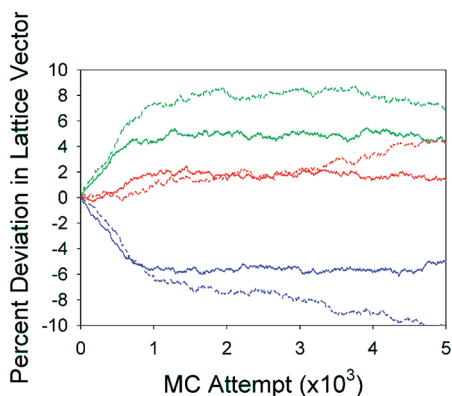
13584

dx.doi.org/10.1021/jp2044064 |*J. Phys. Chem. B* 2011, 115, 13578–13592

Figure 4. Comparison of individual normalized lattice vector evolution for the [MeHyd][NO$_3$] crystal system for simulations which include (solid) and ignore (dashed) the effect of explicit lone pair force centers. The predicted lattice vector normalized by the experimental value is plotted for the a (green), b (blue), and c (red) principle lattice directions.

universally deviate by a roughly 2% absolute magnitude or less. Interestingly, removing an extended charge center (lone pair) on the N$_2$H$_5$$^+$ cation *improves* the reproduction of the [Hyd][NO$_3$] crystal structure. However, removing the extended charge representing a lone pair from the description of (CH$_3$)N$_2$H$_4$$^+$ results in significantly larger deviation of lattice vectors in the [MeHyd][NO$_3$] crystal, as shown in Figure 4. Whether this represents actual instability of the crystal without extended charges or simply far worse reproduction of the lattice vectors while remaining in the same crystal structure is unknown, since the divergent run was terminated before a steady state was reached due to the poor quality of lattice vector reproduction.

Since one of the more important features of the developed force field is its transferability (and subsequent applicability over a range of systems larger than just those in this work), we chose to systematically add the extended charge to all the hydrazinium-based cations due to the significant improvement in reproducing the electrostatic potential. In general we have found that the presence of explicit lone pairs (extended charges) is necessary in a number of the crystals to properly capture the local electrostatic environment of the cation and correct ion packing. In turn, proper representation of the local electrostatic environment of the cation (through inclusion of the explicit lone pairs as well as the many-body polarizability) is sufficient to represent most of the energy of a traditional hydrogen bond.[45]

For [Hyd][N(CN)$_2$], the structural symmetry of the crystal presents a challenge for both the simulation of the system as well as the refinement of the X-ray data. The final crystal structure is in the *Cmcm* space group, which predicts a symmetric orientation for the hydrazinium cations with a 50% fractional occupancy of the excess cationic proton on each nitrogen of the hydrazinium ion. This is an indicator that the relative orientation of the NH$_3$$^+$ group in the hydrazinium is randomized in the crystal, with neither direction being preferred over the other in a perfect crystal. Since fractional occupancy is a statistical effect due to symmetry considerations, we are forced when simulating to settle upon some finite implementation of the random hydrazinium orientations. Earlier calculations of the [Hyd][N(CN)$_2$] crystal structure indicated a *Pnma* structure, whose lattice differs from that of the *Cmcm* structure primarily in the prediction a slightly larger tilt of the N—N hydrazinium axis within the crystal cell, yielding very similar lattice vector magnitudes and unit cell
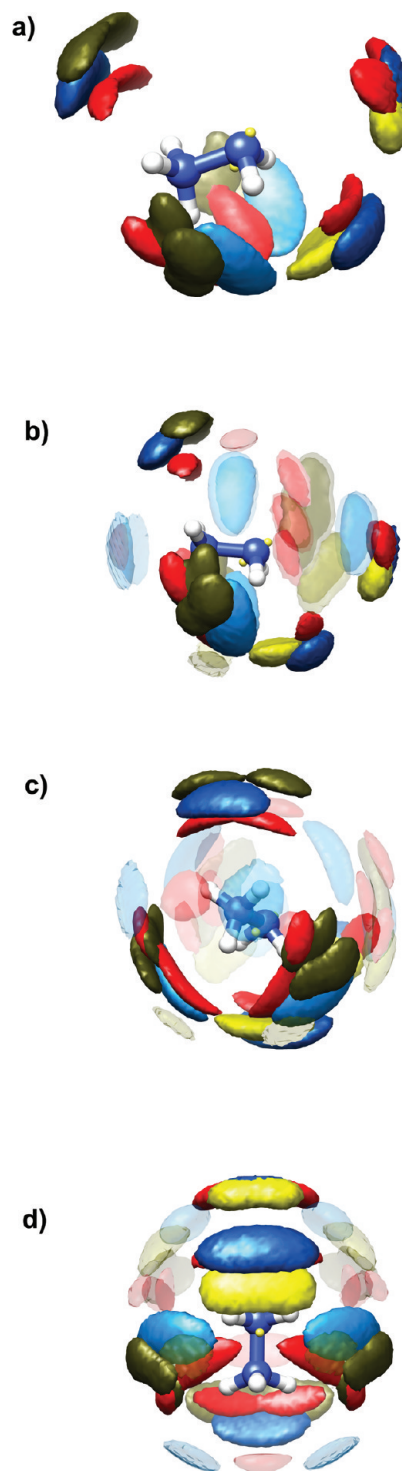

Figure 5. Ion correlations between the hydrazinium cation and all simulated anions. Density isosurfaces represent local amplification of the density of specific atoms of the anions by a factor of 10 over their expected bulk values: oxygen in NO$_3$$^-$ (red), terminal (light blue) and central (dark blue) nitrogens in N(CN)$_2$$^-$, terminal azide (bright yellow), bonded azide (medium gold), and N3/N4 ring (dark gold) nitrogens in CN$_7$$^-$. Part a presents only the density isosurfaces for locations which are fundamentally similar for all three anions, representing the principle locations of hydrogen bonding, while differing views are shown by (b) side, (c) NH$_3$ end, and (d) below with the surfaces of a colored opaquely while secondary locations (all at the same relative density) which differ from anion to anion are represented with transparent versions of the appropriate color.

volume. It is these data from which we took the starting point for our simulations. The presence of the skew within the *Pnma* starting point, coupled with the fact that the proton location is primarily predicted from electron density maps and symmetry considerations, leads to unambiguous placement of the protons within the *Pnma* symmetry, compared to the fractional occupancy of the *Cmcm* group. In practical terms, simulation from the *Pnma* space group starting point reflects a systematic choice of excess proton placement coupled with a slight additional skew relative to the correct *Cmcm* starting point.

For experimental comparison, we present lattice parameters from both the initially calculated *Pnma* crystal structure and the final calculation yielding a *Cmcm* crystal, as comparisons to the simulation. In the case of calculating the percentage differences for the *Cmcm* crystal, the as-provided lattice vectors represented a permuted set of lattice vectors with respect to those simulated (and calculated) for the *Pnma* crystal. For purposes of ease of comparison, we have removed this permutation by transforming the *Cmcm* axes as follows: $\langle a \rangle_{Cmcm} \approx \langle b \rangle_{Pnma}$, $\langle b \rangle_{Cmcm} \approx \langle c \rangle_{Pnma}$, and $\langle c \rangle_{Cmcm} \approx \langle a \rangle_{Pnma}$. This permutation was verified by visual comparison of the structure file of the *Pnma* crystal with that of the *Cmcm* crystal and is wholly unambiguous. We compare the simulation with the properly permuted lattice vectors of the *Cmcm* crystal structure in Table 3. Despite the slight deviation in starting conditions, it can be seen that excellent reproduction of the crystal structure is maintained, indicating that the as-simulated *Pnma* crystal is indeed only a slightly perturbed *Cmcm* structure in the simulated system as well as in the experimental system.

Ion Packing. We have investigated the ion packing for both a series of all three cations given a constant anion (NO_3^-) as well as a series of three anions with a constant cation $(N_2H_5^+)$, using the relative site density amplification of the most negative atoms within the anions, defined by

$$\rho' = \rho(x, y, z)/\rho_{\text{bulk}} \tag{12}$$

where $\rho(x,y,z)$ represents the local site density of the target anion atom in a cubic subvolume of approximately 0.1 Å/side. For the hydrazinium cations, we define the local coordinate system relative to a basis formed by the position of the two nitrogens and the "outward" lone pair (Lp) force center (where the outward lone pair is that which simultaneously has a larger than 90° angle with each of the NH$_2$ N—H bonds as well as the N—N bond). For notational convenience, it will also be of use to define the "top" of the molecule as the half of space which contains the aforementioned outward pair and is bisected by a plane embedding the N—N bond, with normal perpendicular to the N—N bond and residing in the plane that embeds both the N—N and N—outward Lp bond.

We begin by investigating the differences in the hydrogen bonding structure of the $N_2H_5^+$ cation with NO_3^-, CN_7^-, and $N(CN)_2^-$. Figure 5 presents graphs of the 3D density amplification isosurfaces defined in eq 12 with $\rho' = 10$. The differing surface colors represent the negatively charged atomic species for their associated anions (red = O in NO_3^-, blue = N in $N(CN)_2^-$, yellow = N in CN_7^-), with differing brightnesses qualitatively denoting the relative charge magnitude (brighter is more negative). A single red represents the equivalent O in NO_3^- ($q \approx -0.66e$), while light blue ($q \approx -0.68e$) represents terminal and dark blue central ($q \approx -0.62e$) nitrogens in $N(CN)_2^-$. Three shades of gold represent the terminal azide (bright, $q \approx -0.36e$), the bonded azide (medium, $q \approx -0.28e$), and the 3,4 ring (dark, $q \approx -0.25e$) nitrogens of CN_7^-. Figure 5a presents
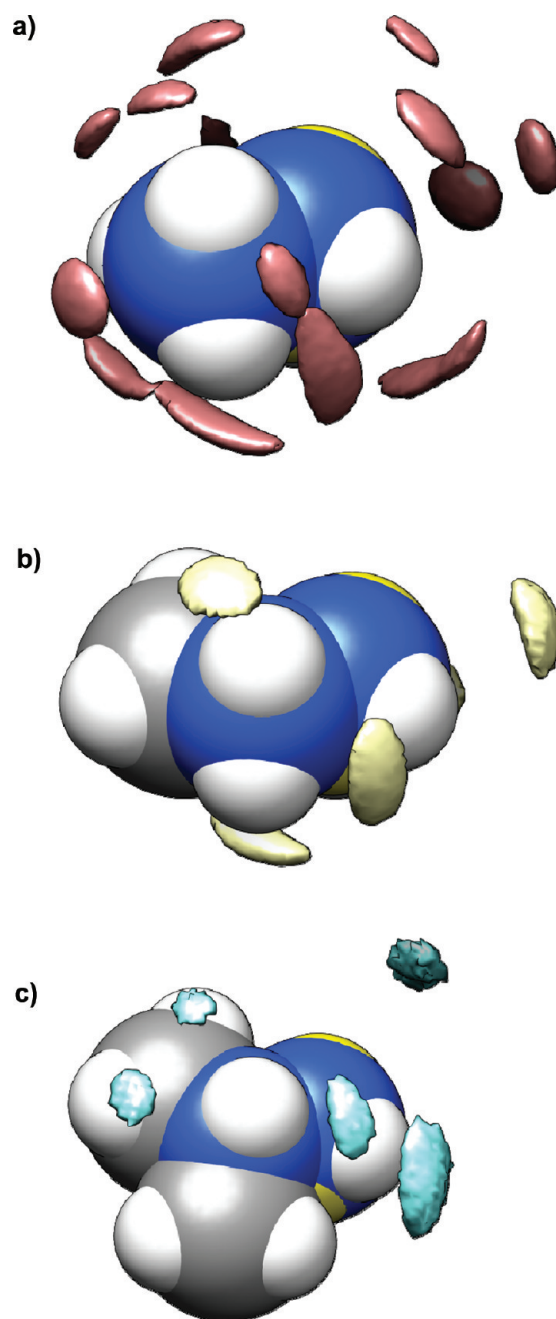
Figure 6. Ion correlations between the hydrazinium cations and the oxygen in the nitrate anions for (a) hydrazinium nitrate, (b) methylhydrazinium nitrate, and (c) dimethylhydrazinium nitrate. Density isosurfaces represent local amplification of oxygen density that is 20 times greater than the bulk density of oxygen in the crystal.

isosurfaces for relative densities that are similar in location across all three anions, representing the primary binding sites driving crystalline interactions. For clarity, Figure 5a presents these isosurfaces for *only* these shared locations, with other locations of similar density but nonshared positions removed. The overwhelming importance of strong hydrogen bonding is clearly seen, since all but one of the shared sites show direct interactions between the anions and the hydrogens of the $N_2H_5^+$ molecule, with the remaining site showing the localization of the negatively charged anion atoms in response to the explicit lone pair.
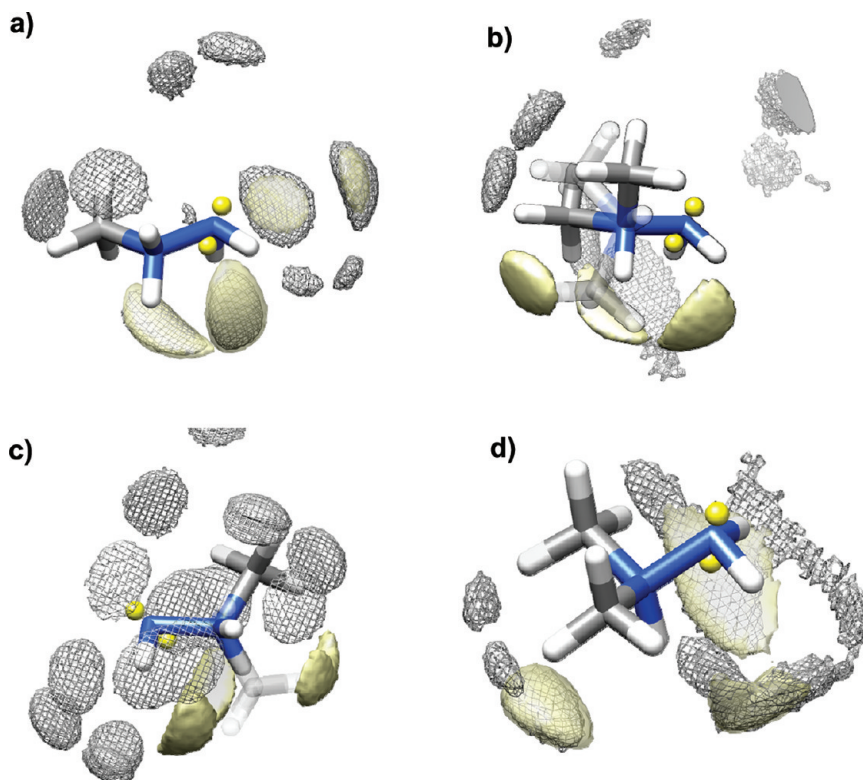
Figure 7. Comparison of ion correlations for crystalline and liquid systems for (a) $[MeHyd][NO_3]$, (b) $[DiMeHyd][NO_3]$, (c) $[MeHyd][N_3]$, and (d) $[DiMeHyd][N_3]$. Crystal correlations are represented by the meshed areas, while liquid correlations by the solid yellow areas. For b and c, the cations undergo conformational changes as the crystal melts, with representative conformations for the crystalline system indicated by transparency in the functional groups which show positional deviation due to the differences in average conformations.

The explicit $N_2H_5^+$ ion depiction is provided as an illustrative frame of reference in orienting the cation relative to the surrounding density isosurfaces, since the NH_3 group shows at least partial torsional mobility with the NO_3^- and CN_7^- anions, while simulation data suggest that $[N_2H_5][N(CN)_2]$ allows the NH_3 group to fully rotate in the crystal. A parallel could be drawn with the recently investigated $[N(CH_3)_4][N(CN)_2]$ plastic crystal that exhibited fast -CH_3 group rotation.[16] Parts b−d of Figure 5 present different viewpoints on the anion binding with the same value of ρ', with the principal binding sites of Figure 5a left solidly colored, while ancillary binding sites are left transparent. In this case, we believe all of the transparent sites represent the effective binding due to simultaneous optimization of steric and packing constraints coupled with maximization of charge-based interactions.

While we cannot quantify the overall relative contributions of any specific interactions via this technique, we believe the principle interactions highlighted in Figure 5a arising from strong hydrogen bonding are the most fundamental in determining the crystal structure. As evidence, we consider the cases of both the $(CH_3)N_2H_4^+$ and $(CH_3)_2N_2H_3^+$ cations with N_3^- and NO_3^- counterions. In neither case can we construct graphs such as Figure 5, since each cation has one of the two crystalline forms which stabilizes with the central N−N torsional angle perturbed from the lowest energy state in the gas phase ($[(CH_3)N_2H_4][N_3]$ and $[(CH_3)_2N_2H_3][NO_3]$ each show this effect). The freezing in of a higher conformational energy state to allow more facile hydrogen bonding is indicative of the overall importance of the hydrogen bonding interaction in stabilizing the crystalline system.

To understand the effect of progressive methylation, we investigate the correlation of the oxygen in NO_3^- with the hydrazinium cations, using a density amplification factor of $\rho' = 20$ shown in Figure 6. Figure 6a represents $[N_2H_5][NO_3]$; Figure 6b, $[(CH_3)N_2H_4][NO_3]$; and Figure 6c, $[(CH_3)_2N_2H_3]-[NO_3]$. In each panel, the principle interaction is the coordination of an oxygen by multiple hydrogens. For the unmethylated cation, coordination appears to occur by only two hydrogens, with the exception of the basal plane of the pyramidal structure formed by the NH_3 group with the other nitrogen in $N_2H_5^+$, where an oxygen is coordinated by all three hydrogens of the NH_3 group. As methylation proceeds, the magnitude of the hydrogen charge on the methylated groups is reduced, which leads to preferential coordination by three hydrogens in response to the weakening of the magnitude of the hydrogen−oxygen interaction with the methyl hydrogens. There is also a trend for coordination locations to push toward the center of the cation with increasing methylation. This may be due to steric considerations involving the larger methyl groups, a preference for the oxygens to migrate toward coordination with the more strongly charged hydrogens attached directly to the nitrogen of the cations, or both. The only significant deviation from preferring strong hydrogen bonding locations occurs at the NH_2 end of each cation, and, as in Figure 5, appears to be a response to minimizing the anion−lone pair interaction while still maintaining some interaction with the NH_2 group hydrogen.

Where possible, we have also investigated the difference in coordination between liquid and crystalline systems. For $[N_2H_5]-[CN_7]$ decomposition occurs within the solid phase before

13587

dx.doi.org/10.1021/jp2044064 |*J. Phys. Chem. B* 2011, 115, 13578–13592

Table 4. Elastic Constants and Bulk Moduli of $[N_2H_5][NO_3]$ at 120 K (All values in GPa)

	C_{xy}					
	$y = 1$	$y = 2$	$y = 3$	$y = 4$	$y = 5$	$y = 6$
$x = 1$	43.0 ± 0.6	26.2 ± 0.6	28.0 ± 0.4	3.0 ± 0.2	1.4 ± 0.3	-1.5 ± 0.5
$x = 2$		43.5 ± 1.0	23.5 ± 0.9	2.0 ± 0.1	4.8 ± 0.3	-1.1 ± 0.5
$x = 3$			106.5 ± 2.5	2.2 ± 0.4	-3.5 ± 0.7	-2.8 ± 0.6
$x = 4$				22.3 ± 0.3	-1.3 ± 0.1	3.2 ± 0.2
$x = 5$					21.0 ± 0.1	-0.4 ± 0.3
$x = 6$						22.1 ± 0.4

bulk modulus (K)				shear modulus (G)			
Voigt	38.7 ± 0.4	Reuss	20.8 ± 0.3	Voigt	33.1 ± 0.6	Reuss	16.5 ± 0.1

Table 5. Elastic Constants and Bulk Moduli of $[(CH_3)N_2H_4][NO_3]$ at 200 K (All values in GPa)

	C_{xy}					
	$y = 1$	$y = 2$	$y = 3$	$y = 4$	$y = 5$	$y = 6$
$x = 1$	38.2 ± 0.5	19.8 ± 0.5	12.3 ± 0.4	-0.2 ± 0.4	0.7 ± 0.2	-1.6 ± 0.2
$x = 2$		39.1 ± 0.6	22.8 ± 0.5	-0.4 ± 0.3	-3.5 ± 0.1	-2.1 ± 0.1
$x = 3$			37.4 ± 0.4	-1.4 ± 0.2	-6.1 ± 0.1	-1.6 ± 0.2
$x = 4$				21.9 ± 0.2	1.0 ± 0.2	-3.1 ± 0.2
$x = 5$					7.3 ± 0.1	1.2 ± 0.1
$x = 6$						9.6 ± 0.2

bulk modulus (K)				shear modulus (G)			
Voigt	24.9 ± 0.3	Reuss	23.0 ± 0.3	Voigt	11.7 ± 0.1	Reuss	8.8 ± 0.1

melting occurs, while for the $[N_2H_5][N(CN)_2]$ system facile isomerization to guanazole occurs at temperatures well below the melting temperature, leading to the expectation that pure $[N_2H_5]$-$[N(CN)_2]$ in the liquid phase is nearly or totally nonexistent.[46] For $[N_2H_5][NO_3]$, while a liquid phase is known to exist experimentally, we were unable to simulate such a system due to overly strong interactions between the acidic hydrogen atoms of the NH_3^+ group, which attack either the lone pair attached to nearby hydrazinium atoms or oxygens of nearby NO_3^- ions. For the remaining $(CH_3)N_2H_4^+$ and $(CH_3)_2N_2H_3^+$ cations in concert with the NO_3^- and N_3^- anions, we compare the structure from the crystal at experimentally observed temperatures with that of a liquid at 353 K. The liquid simulation was run for a minimum of 6 ns, and the local site density enhancement of anion correlations calculated as above (O for NO_3^-, terminal nitrogens for N_3^-). Figure 7 presents the comparison of observed anion site densities in the liquid and crystalline phases for each calculable system. In both $[(CH_3)N_2H_4][NO_3]$ and $[(CH_3)_2N_2H_3][N_3]$ (Figure 7a,d) the differences between crystal and liquid packing are rather small, with the relaxed steric constraints of the liquid phase allowing the anions to interact primarily through the acidic hydrogens attached directly to the nitrogens, rather than forcing interaction with the only slightly charged hydrogens of the methyl groups as seen in the crystals. Both $[(CH_3)_2N_2H_3][NO_3]$ and $[(CH_3)$-$N_2H_4][N_3]$ (Figure 7b,c) show significantly larger differences between the crystal and liquid phases, due to the aforementioned conformations in the crystal phase which are not the lowest energy conformer. For these salts, the crystalline conformation

shows a methyl group in the trans position relative to the upward lone pair of the NH_2 group (represented by the transparently depicted groups in Figure 7b,c), which serves the effect of exposing the acidic hydrogens on the substituted N^+ atom to interaction with anionic groups from multiple angles, allowing the crystal to stabilize. In the liquid phase, where accommodation of strong steric interactions loses importance, the cations regain their standard low-energy conformation with hydrogens, rather than methyl groups, in the trans position. This is especially notable in the $[(CH_3)N_2H_4][N_3]$, where, keeping the N^+-N-Lp basis as constant, the difference in conformation leads to a near total inversion in the spatial location of primary anion association near the N^+ atom. For both of these systems, the net effect is a far larger localization of anionic countercharge in the liquid phase compared to the crystalline phase.

Mechanical Properties. To calculate the mechanical properties of the crystals, we employ the formalism of Parinello and Rahman,[47] which relates the elastic stiffness tensor (ε) to the fluctuations in the elastic strain tensor of the material given by the upper-triangular matrix (denoted as $\mathbf{h}$) which embeds the lattice vectors of the instantaneous unit cell within its columns:

$$\varepsilon = \frac{1}{2}\left((\mathbf{h}_0')^{-1}\mathbf{h}'\mathbf{h}\mathbf{h}_0^{-1} - 1\right) \tag{13}$$

Here a prime symbol ($'$) denotes a matrix transpose, and $\mathbf{h}_0$ represents the reference unit cell of the system, which is taken to be an average over all of the unit cell fluctuations once a steady-state configuration has been reached. Expression of the

Table 6. Elastic Constants and Moduli of $[(CH_3)_2N_2H_3][NO_3]$ at 200 K (All Values in GPa)

| | C_{xy} | | | | | |
	$y = 1$	$y = 2$	$y = 3$	$y = 4$	$y = 5$	$y = 6$
$x = 1$	19.2 ± 0.3	9.3 ± 0.1	8.3 ± 0.2	-1.2 ± 0.1	-1.0 ± 0.1	-0.7 ± 0.1
$x = 2$		18.5 ± 0.3	7.4 ± 0.2	1.5 ± 0.2	0.1 ± 0.1	0.3 ± 0.0
$x = 3$			11.6 ± 0.1	-0.3 ± 0.1	0.5 ± 0.1	-1.0 ± 0.0
$x = 4$				7.0 ± 0.2	1.5 ± 0.1	1.1 ± 0.1
$x = 5$					6.7 ± 0.1	0.6 ± 0.0
$x = 6$						4.3 ± 0.1

bulk modulus (K)				shear modulus (G)			
Voigt	11.0 ± 0.1	Reuss	10.0 ± 0.1	Voigt	5.2 ± 0.0	Reuss	4.4 ± 0.0

Table 7. Elastic Constants and Bulk Moduli of $[N_2H_5][N(CN)_2]$ at 173 K (All values in GPa)

| | C_{xy} | | | | | |
	$y = 1$	$y = 2$	$y = 3$	$y = 4$	$y = 5$	$y = 6$
$x = 1$	53.7 ± 0.4	27.0 ± 0.6	20.8 ± 0.4	0.1 ± 0.1	-0.1 ± 0.1	-1.1 ± 0.3
$x = 2$		92.9 ± 1.0	21.2 ± 0.6	-0.2 ± 0.1	-2.2 ± 0.4	1.9 ± 0.5
$x = 3$			43.3 ± 0.6	-0.5 ± 0.2	0.5 ± 0.2	-0.6 ± 0.3
$x = 4$				11.1 ± 0.1	-0.1 ± 0.1	-0.1 ± 0.1
$x = 5$					12.5 ± 0.3	0.6 ± 0.1
$x = 6$						10.4 ± 0.2

bulk modulus (K)				shear modulus (G)			
Voigt	36.4 ± 0.4	Reuss	32.7 ± 0.4	Voigt	14.8 ± 0.1	Reuss	13.0 ± 0.1

compliance tensor (S_{ijkl}) in terms of the outer product of the strain fluctuations

$$S_{ijkl} = \langle \varepsilon_{ij} \otimes \varepsilon_{kl} \rangle \frac{\langle V \rangle}{k_B T} \tag{14}$$

(with V being the instantaneous unit cell volume, k_B Boltzmann's constant, and T the temperature) allows for the calculation of the elastic stiffness tensor (C_{ijkl}) as the matrix inversion of the compliance tensor, provided the contracted stress and strain vectors are suitably defined.[48]

We have performed these calculations on all seven of our simulated crystals, with the resulting elastic constants as well as the Reuss and Voigt estimates of bulk and shear moduli[49] reported in Tables 4—10. Since simulations occurred at different temperatures, a direct comparison among the entirety of the data is problematic. The two significant outliers for temperature are the $[N_2H_5][NO_3]$ system at 120 K and the $[N_2H_5][CN_7]$ system at 100 K. The remainder of the systems fall at either 173 or 200 K, both of which are close enough relative to the other to expect qualitative trends to be accurate. In addition, it is reasonable to expect that the experimental conditions for the unambiguous determination of crystal structure represents a rough regime of "normal" solid handling conditions which might be representative of the behavior of the crystalline systems in actual utilization. Under the second assumption, we are able to qualitatively compare the crystals using their bulk and shear moduli. The bulk moduli give the relative order of

$[N_2H_5][CN_7] > [N_2H_5][N(CN)_2] \approx [N_2H_5][NO_3] > [(CH_3)N_2H_4][NO_3] \approx [(CH_3)N_2H_4][N_3] > [(CH_3)_2N_2H_3][N_3] > [(CH_3)_2N_2H_3][NO_3]$. The general trend here shows a decrease in the bulk modulus as methylation is increased, likely due to the loss of the stronger hydrogen bonding associated with hydrogens attached directly to the nitrogen instead of through an intermediary methyl carbon. In the nitrate-containing crystals for which we have a complete series of cations, the effect of adding a methyl group to the crystal seems to be the lowering of the bulk modulus by roughly 10 GPa. While the general trends of decreasing magnitude with increasing methylation persist in the shear moduli, the overall order of the moduli differs from the bulk, yielding $[N_2H_5][NO_3] > [N_2H_5][CN_7] > [N_2H_5][N(CN)_2] \approx [(CH_3)N_2H_4][NO_3] > [(CH_3)N_2H_4][N_3] \approx [(CH_3)_2N_2H_3][NO_3] \approx [(CH_3)_2N_2H_3][N_3]$. In all cases the shear modulus is lower for each compound than the corresponding bulk modulus, with the ratios of shear to bulk modulus varying from roughly 80% ($[N_2H_5][NO_3]$) down to roughly 25% ($[(CH_3)_2N_2H_3][N_3]$). While the bulk moduli tend to indicate that a larger anion leads to larger modulus, the same trend does not hold true for the shear moduli. This is likely to be due to the directionally specific nature of shear, when compared to bulk, which is an isotropic property. For example, while it makes sense to believe that a larger anion (such as CN_7^-) can reinforce the bulk modulus simply by providing more steric volume to resist distortions, consideration of the actual shape (planar) of the anion becomes important in shear, where much

13589

dx.doi.org/10.1021/jp2044064 |*J. Phys. Chem. B* 2011, 115, 13578–13592

Table 8. Elastic Constants and Bulk Moduli of $[N_2H_5][NO_3]$ at 100 K (All values in GPa)

	C_{xy}					
	$y = 1$	$y = 2$	$y = 3$	$y = 4$	$y = 5$	$y = 6$
$x = 1$	60.0 ± 1.1	14.6 ± 0.8	39.8 ± 0.9	-0.8 ± 0.2	21.3 ± 0.5	-0.1 ± 0.1
$x = 2$		90.8 ± 0.9	38.3 ± 0.9	1.4 ± 0.2	-2.7 ± 0.5	-0.3 ± 0.1
$x = 3$			63.0 ± 0.9	-1.9 ± 0.2	17.6 ± 0.5	-2.0 ± 0.1
$x = 4$				6.1 ± 0.1	-2.3 ± 0.1	0.3 ± 0.1
$x = 5$					37.5 ± 0.4	0.9 ± 0.1
$x = 6$						9.6 ± 0.1

bulk modulus (K)			shear modulus (G)		
Voigt	44.4 ± 0.8	Reuss	37.1 ± 0.7	Voigt	18.7 ± 0.1	Reuss	10.6 ± 0.1

Table 9. Elastic Constants and Bulk Moduli of $[(CH_3)N_2H_4][N_3]$ at 200 K (All values in GPa)

	C_{xy}					
	$y = 1$	$y = 2$	$y = 3$	$y = 4$	$y = 5$	$y = 6$
$x = 1$	48.1 ± 0.7	23.7 ± 0.7	27.7 ± 0.6	-3.1 ± 0.1	-0.8 ± 0.2	2.3 ± 0.2
$x = 2$		34.2 ± 0.9	20.1 ± 0.6	-0.6 ± 0.0	-0.6 ± 0.2	0.4 ± 0.2
$x = 3$			23.4 ± 0.5	-1.7 ± 0.1	-1.6 ± 0.2	-0.9 ± 0.2
$x = 4$				6.6 ± 0.0	2.8 ± 0.0	-1.4 ± 0.1
$x = 5$					5.6 ± 0.1	-0.1 ± 0.1
$x = 6$						7.9 ± 0.2

bulk modulus (K)			shear modulus (G)		
Voigt	27.6 ± 0.6	Reuss	20.8 ± 0.6	Voigt	6.3 ± 0.0	Reuss	4.0 ± 0.0

Table 10. Elastic Constants and Moduli of $[(CH_3)_2N_2H_3][N_3]$ at 173 K (All Values in GPa)

	C_{xy}					
	$y = 1$	$y = 2$	$y = 3$	$y = 4$	$y = 5$	$y = 6$
$x = 1$	29.7 ± 0.4	8.7 ± 0.3	20.4 ± 0.4	0.3 ± 0.1	-2.7 ± 0.1	3.0 ± 0.3
$x = 2$		18.3 ± 0.1	11.6 ± 0.2	-3.5 ± 0.1	-1.1 ± 0.1	1.4 ± 0.2
$x = 3$			22.7 ± 0.3	-1.0 ± 0.1	-1.2 ± 0.1	2.3 ± 0.2
$x = 4$				3.7 ± 0.0	-1.1 ± 0.0	1.2 ± 0.1
$x = 5$					2.8 ± 0.1	0.9 ± 0.1
$x = 6$						4.7 ± 0.2

bulk modulus (K)			shear modulus (G)		
Voigt	16.9 ± 0.4	Reuss	7.8 ± 0.4	Voigt	4.3 ± 0.1	Reuss	1.9 ± 0.1

of that bulk is minimized if the molecule is subjected to forces which lie in the plane of the anion.

V. CONCLUDING REMARKS

Utilizing a many-body polarizable formulation with explicit lone pairs, we have parametrized a transferrable, consistent force field to represent the hydrazinium cation and its monomethyl and unsymmetrically dimethylated derivatives in conjunction with N_3^-, NO_3^-, $N(CN)_2^-$, and CN_7^-. We have simulated seven hydrazinium-based crystals with four differing anionic species, with most predictions showing excellent volumetric parity with experiment, on a range of $\sim$2.5% or less, with individual lattice vector deviation of $\sim$1–6%. For the $[N_2H_5]$-$[NO_3]$ crystal volumetric deviation is $\sim$6%, and for the $[(CH_3)$-$N_2H_4][N_3]$ crystal, $\sim$7%, with individual lattice vectors in the 1–7% range. Of particular interest in the case of the cations is the necessity of including lone pairs to accurately reproduce the local electrostatic field of these ions near the NH_2 group. While addition of off-atom charges to represent lone pairs is often

suggested for both anions and certain neutral molecules, the necessity of their presence on a cationic species is noteworthy. We have also performed liquid-state simulations of the neutral hydrazines, as well as the NO_3^-- and N_3^--based ionic salts. Comparison of the hydrazines shows excellent reproduction of both density and heat of vaporization at room temperature, with density reproduction drifting for the pure hydrazine at elevated temperatures, while predictions for $(CH_3)N_2H_3$ and $(CH_3)_2$-N_2H_2 remain stable.

Quantum chemistry geometry optimizations performed at the MP2/cc-pvTz theory level starting with the cation−anion configurations of $[N_2H_5][NO_3]$, $[N_2H_5][CN_7]$, $[(CH_3)N_2H_4]$-$[NO_3]$, $[(CH_3)N_2H_4][N_3]$, and $[(CH_3)_2N_2H_4][N_3]$ resulted in a proton transfer from the cation to anion and formation of the neutral species in the gas phase. For the $[N_2H_5][NO_3]$ pair calculation, we have also performed QC calculations using polarizable continuum solvation model, noting that placing the deionized pair into a polarizable continuum leads to reionization of the constituent neutral molecules. MP2/cc-pvTz calculations of the $([N_2H_5][NO_3])_2$ complex also yielded ionic species in accord with the crystal being ionic. We believe this is indicative of the fact that while *isolated* ion pairs are unstable, bulk phase ionic liquids are effectively stabilized in the ionic state due to the dielectric medium of the surrounding ionic liquid as well as due to formation of the hydrogen bonding network

It is noteworthy that, of the seven crystals we simulated, we see the largest deviation in those that have the smallest anions. Furthermore, the quality of prediction seems to systematically increase with increasing methylation of the hydrazinium cations. Coupled with the above discussions of results in the QC calculations, and noting that we parametrize the charge and polarizability each from the *isolated* gas phase, we believe it may be likely that overly strong charge and/or polarization interactions with respect to the acidic hydrogens on the N^+ atoms are responsible for the undesirable force field behavior. As the molecular structures inherently begin to further screen these interactions (either through increased methylation of the cation or increasing anion size, both of which impedes close approach to the acidic hydrogens in the bulk), the undesirable behavior goes away. This would be consistent with the observation that $[(CH_3)N_2H_4][NO_3]$ yields better results than $[(CH_3)N_2H_4]$-$[N_3]$, since N_3^- is smaller than NO_3^- and thus more able to attack the hydrogens near the methyl group of $(CH_3)N_2H_4^+$, as well as the better quality results of $[(CH_3)_2N_2H_3][N_3]$ over $[(CH_3)N_2H_4]$-$[N_3]$ and $[(CH_3)N_2H_4][NO_3]$ over $[N_2H_5][NO_3]$.

Investigation of anion bonding similarities with a common $N_2H_5^+$ across crystals with three differing anions demonstrates the importance of hydrogen bonding in stabilizing the various crystals. We found significant differences between hydrazinium cation coordination by anions in the crystal and liquid phase, indicating that the liquid structure should be inferred from the crystal structure with caution. Structural features such as the hydrogen bonding network and ion sizes and shapes were correlated with the bulk and shear moduli of ionic crystals.

ASSOCIATED CONTENT

Ⓢ Supporting Information. Text describing the determination of the $[N_2H_5][N(CN)_2]$ crystal structure, a table listing crystal and structure refinement data for hydrazinium dicyanamide, and a figure showing an ORTEP diagram of the conformation and atom numbering scheme of hydrazinium dicyanamide.

This material is available free of charge via the Internet at http://pubs.acs.org.

AUTHOR INFORMATION

Corresponding Author
*E-mail: jbhooper@wasatchmolecular.com

ACKNOWLEDGMENT

REFERENCES

(1) Schmidt, E. W. *Hydrazine and Its Derivatives: Preparation, Properties, Applications*, 2nd ed.; John Wiley & Sons: New York, 2001.

(2) Zung, L. B.; Tkachencko, E. A.; Breen B. P. *A Basic Study on the Ignition of Hypergolic Liquid Propellants*, NASA Technical Report No. CR-100387, November 1968; NASA: Washington, DC, 1968.

(3) Price, T. W.; Evans, D. D. *The Status of Monopropellant Hydrazine Technology*, NASA Technical Report No. CR-92742, February 1968; NASA: Washington, DC, 1968.

(4) Toth, B. *J. Cancer Res. Clin. Oncol.* **1980**, *97*, 1432.

(5) Kinkead, E. R.; Haun, C. C.; Vernot, E. H.; MacEwen, J. D. *A Chronic Inhalation Toxicity Study of Monomethylhydrazine*, AFAMRL Technical Report No. TR-85-025; Air Force Aerospace Medical Research Lab: Wright-Patterson Air Force Base, OH, 1985.

(6) Forsyth, S. M.; Pringle, J. M.; MacFarlane, D. R. *Aust. J. Chem.* **2004**, *57*, 113.

(7) Smiglak, M.; Matlen, A.; Rogers, R. D. *Acc. Chem. Res.* **2007**, *40*, 1182.

(8) Schneider, S.; Hawkins, T.; Rosander, M.; Vaghjiani, G.; Chambreau, S.; Drake, G. *Energy Fuels* **2008**, *22*, 2871.

(9) Chambreau, S. D.; Schneider, S.; Rosander, M.; Hawkins, T.; Gallegos, C. J.; Pastewait, M. F.; Vaghjiani, G. L. *J. Phys. Chem. A* **2008**, *112*, 7816.

(10) Schneider, S.; Hawkins, T.; Rosander, M.; Mills, J.; Vaghjiani, G.; Chambreau, S. *Inorg. Chem.* **2008**, *47*, 6082.

(11) Zhang, Y.; Gao, H.; Guo, Y.; Joo, Y. H.; Shreeve, J. M. *Chem.—Eur. J.* **2010**, *16*, 3114.

(12) Klapotke, T. M.; Stierstorfer, J. *J. Am. Chem. Soc.* **2009**, *131*, 1122.

(13) Singh, R. P.; Verma, R. D.; Meshri, D. T.; Shreeve, J. M. *Angew. Chem., Int. Ed.* **2006**, *45*, 3584.

(14) Joo, Y. H.; Gao, H.; Zhang, Y.; Shreeve, J. M. *Inorg. Chem.* **2010**, *49*, 3282.

(15) Borodin, O. *J. Phys. Chem. B* **2009**, *113*, 11467.

(16) Hooper, J. B.; Borodin, O. *Phys. Chem. Chem. Phys.* **2010**, *12*, 4635.

(17) Gutowski, K. E.; Gurkan, B.; Maginn, E. J. *Pure Appl. Chem.* **2009**, *81*, 1799.

(18) Grigoriev, M. S.; Moisy, P.; Auwer, C. D.; Charushnikova, I. A. *Acta Crystallogr.* **2005**, *E61*, i216.

(19) de Bonn, O.; Hammerl, A.; Klapotke, T. M.; Mayer, P.; Piotrowski, H.; Zewen, H. Z. *Anorg. Allg. Chem.* **2001**, *627*, 2011.

(20) Hammerl, A.; Holl, G.; Hubler, K.; Kaiser, M.; Klapotke, T. M.; Mayer, P. *Eur. J. Inorg. Chem.* **2001**, *2001*, 755.

(21) Klapotke, T. M.; Noth, H.; Schewnk-Kircher, H.; Walther, W. H.; Holl, G. *Polyhedron* **1999**, *18*, 717.

(22) Thole, B. T. *Chem. Phys.* **1981**, *59*, 341.

(23) van Duijnen, P. T.; Swart, M. *J. Phys. Chem. A* **1998**, *102*, 2399.

(24) Feenstra, K. A.; Hess, B.; Berendsen, H. J. C. *J. Comput. Chem.* **1999**, *20*, 786.

(25) Jorgensen, W. L.; Chandresekhar, J.; Madura, J. D.; Impey, R. W.; Klein, M. L. *J. Chem. Phys.* **1983**, *79*, 926.

(26) Lopes, P. E. M; Lamoureux, G; Mackerell, A. D. *J. Comput. Chem.* **2009**, *30*, 1821.

(27) Morita, A.; Kato, S. *J. Chem. Phys.* **1999**, *110*, 11987.

(28) Borodin, O.; Smith, G. D. *J. Phys. Chem. B* **2006**, *110*, 6293.

(29) Kaminski, G. A.; Stern, H. A.; Berne, B. J.; Friesner, R. A *J. Phys. Chem. A* **2004**, *108*, 621.

(30) Stout, J. M.; Dykstra, C. E. *J. Phys. Chem. A* **1998**, *102*, 1576.

(31) Kassimi, N. E. B.; Thakkar, A. *J. Chem. Phys. Lett.* **2009**, *472*, 232.

(32) Bedrov, D.; Borodin, O.; Smith, G. D.; Sewell, T. D.; Dattelbaum, D. M.; Stevens, L. L. *J. Chem. Phys.* **2009**, *131*, 224703.

(33) Tomasi, J.; Mennucci, B.; Cammi, R. *Chem. Rev.* **2005**, *105*, 2999.

(34) Stoimenovski, J.; Izgorodina, E. I.; MacFarlane, D. R. *Phys. Chem. Chem. Phys.* **2010**, *12*, 10341.

(35) http://www.wasatchmolecular.com.

(36) http://www.eng.utah.edu/~gsmith/lucretius.html.

(37) Palmer, B. J. *J. Comput. Phys* **1993**, *104*, 470.

(38) Martyna, G. J.; Tuckerman, M. E.; Tobias, D. J.; Klein, M. L. *Mol. Phys.* **1996**, *87*, 1117.

(39) Borodin, O.; Smith, G. D.; Sewell, T. D.; Bedrov, D. *J. Phys. Chem. B* **2008**, *112*, 734.

(40) Sewell, T. D.; Menikoff, R.; Bedrov, D.; Smith, G. D. *J. Chem. Phys.* **2003**, *119*, 7417.

(41) Ahlert, R. C.; Bauerle, G. L.; Lecce, J. V. *J. Chem. Eng. Data* **1962**, *7*, 158.

(42) Ahlert, R. C.; Shimalla, C. J. *J. Chem. Eng. Data* **1968**, *13*, 108.

(43) Lee, A.; Law, C. K.; Makino, A. *Combust. Flame* **1989**, *78*, 263.

(44) Starovoytov, O.; Hooper, J. B.; Borodin, O.; Smith, G. D. Submitted for publication in *J Phys Chem B*.

(45) Stone, A. *The Theory of Intermolecular Forces*; Oxford University Press: Oxford, U.K., 1996.

(46) Frankel, M. B.; Burns, E. A.; Butler, J. C.; Wilson, E. R. *J. Org. Chem.* **1963**, *28*, 2428.

(47) Parrinello, M.; Rahman, A. *J. Chem. Phys.* **1982**, *76*, 2662.

(48) Tsai, S. W.; *Mechanics of Composite Materials, Part II, Theoretical Aspects*, AFML Technical Report No. AFMLTR-66-149, November 1966; Air Force Materials Laboratory: Wright-Patterson Air Force Base, OH, USA, 1966.

(49) Hill, R. *Proc. Phys. Soc. A* **1952**, *65*, 349.

13592

dx.doi.org/10.1021/jp2044064 |*J. Phys. Chem. B* 2011, 115, 13578–13592